



HYPERVELOCITY IMPACT ON CARBON FIBRE REINFORCED PLASTIC / ALUMINIUM HONEYCOMB: COMPARISON WITH WHIPPLE BUMPER SHIELDS

E. A. TAYLOR, M. K. HERBERT, B. A. M. VAUGHAN and
 J. A. M. MCDONNELL

Unit for Space Sciences and Astrophysics, School of Physical Sciences, University of Kent at Canterbury,
 Canterbury, Kent, CT2 7NR, U. K.

Summary—Normal and oblique incidence hypervelocity impact tests (velocity range 4–6 km s⁻¹) were carried out to determine the ballistic limit of a 1.6 mm carbon fibre reinforced plastic facesheet bonded to 45 mm aluminium honeycomb core, as typically used in Low Earth Orbiting spacecraft. The internal honeycomb damage was determined as a function of the impactor parameters. The ballistic limit data showed a strong dependence with impact angle. The internal honeycomb damage was found to be independent of impact angle for constant impact energy for $\Theta < 50^\circ$. An empirically-determined damage equation linking honeycomb damage to impact energy was developed. For the highest impact energy perforating impacts, the debris cone angles for the primary and secondary debris cones were determined. As the impact angle increased, the centre of the damage cones rotated away from the line of flight. The data have been compared with the ballistic limit curve defined by the modified Cour-Palais aluminium Whipple bumper equation and show broad agreement with the equation predictions. A reduced value of the rear facesheet thickness is required to bring the normal and 15° incidence data into agreement with the ballistic limit curve.

© 1999 Elsevier Science Ltd. All rights reserved.

NOTATION

Al-HC	Aluminium Honeycomb	D_{eq}	(Equivalent) Diameter of CFRP hole (mm)
CFRP	Carbon Fibre Reinforced Plastic	D_{dam}	Honeycomb blast damage area (mm ²)
LEO	Low Earth Orbit	D_{prim}	Primary cone diameter (mm)
LGG	Light Gas Gun	D_{sec}	Secondary cone diameter (mm)
LOF	Line of Flight	d_{crit}	Critical diameter for perforation (cm)
L/D	Length/Diameter	d_p	Projectile diameter (mm)
MLI	Multi-Layer Insulation	E	Impact energy (J)
NP	Non-Perforating	t_b	Bumper thickness (cm)
P	Perforating	t_w	Back-up wall thickness (cm)
		S	Whipple spacing (cm)
α	Primary cone angle (°)	A_h	Area of CFRP hole (mm ²)
β	Secondary cone angle (°)	A_f	Area of CFRP hole (front) (mm ²)
ϵ	Turning angle (°)	A_r	Area of CFRP hole (rear) (mm ²)
Θ, θ	Impact angle (°)		
V, v	Impact velocity (km s ⁻¹)		
ρ_p	Projectile density (g cm ⁻³)		
ρ_b	Back-wall density (g cm ⁻³)		
σ	Yield strength of back-up wall (ksi)		

INTRODUCTION

Spacecraft external walls are typically made of aluminium honeycomb core and an aluminium or woven composite material (CFRP) facesheet, bonded to the core using a resin. This material (referred to as spacecraft honeycomb) provides good performance in terms of high strength, low weight and low thermal distortion and, augmented by externally-mounted multi-layer insulation,

provides the primary shielding protection against space debris and meteoroid particle impact for unmanned spacecraft. The predicted increase in the LEO space debris population (linked to the rise in total satellite mass launched), correlated with the increase in average satellite size, has meant that the issue of hypervelocity impact onto spacecraft honeycomb is of increasing concern. Impact tests are required to characterise the hypervelocity impact response of the honeycomb, as computational modelling of hypervelocity impacts onto honeycomb is at an early stage [1]. However, ground based tests are not possible over the whole range of impactor conditions (typical parameters: velocity range 5–20 km s⁻¹, density 1–8 g cm⁻³, impact angle 0°–75°), so experimental data must be used to develop a predictive damage equation which can be extrapolated to LEO impact conditions.

The response of spacecraft honeycomb to hypervelocity impact has been poorly characterised to date. Previous work in this field focused initially on the use of honeycomb for manned spacecraft, quantifying the hazard due to meteoroid impact. Cadmium shields were therefore used to investigate impacts onto equivalent aluminium shields at impact velocities > 7 km s⁻¹ with the honeycomb represented by a 6061-T6 aluminium cylinder. Channelling was observed and the cell wall thickness was found not to significantly affect the impact performance of the target [2]. Tests on different aluminium alloys - 2024, 5052 and 7075 - as honeycomb cell-equivalent cylinders, showed no significant difference in their performance [3]. Tests were carried out on honeycombs with deep cores (equivalent to large Whipple bumper spacings) and the influence of the cell diameter on the required rear sheet thicknesses for prevention of perforation was investigated [3].

The channelling action of the honeycomb was also investigated for 0°, 45° and 60° incidence shots [4]. 4.76 mm Lexan cylinders were fired onto 24.1 mm thick aluminium honeycomb. For the velocity range tested (3–7 km s⁻¹), the debris clouds produced contained primarily solid fragments. The velocity required to reach the ballistic limit of the structure rose from 4.3 to 7.2 km s⁻¹ as the impact angle was increased from 0° to 60°, with a velocity of 6.7 km s⁻¹ required to perforate at 45° incidence. Note that, unlike the previous tests, 'real' hexagonal honeycomb was used instead of equivalent diameter cylinders. Shots onto honeycomb beyond the ballistic limit were also carried out for honeycomb placed outside nickel-hydrogen batteries and Space Station radiator panels [5, 6]. For impacts beyond the ballistic limit, the facesheet is delaminated from the honeycomb core and the whole structure is warped. Impact tests have also been carried out onto CFRP facesheet/aluminium honeycomb covered with a layer of MLI [7, 8, 9, 10]. The addition of MLI has been shown to increase significantly the ballistic limit of the honeycomb structure. No direct comparison between the performance of aluminium and CFRP honeycombs has yet been made and a damage equation incorporating the target parameters - honeycomb depth, cell size, cell wall thickness, alloy type, bumper and back-up wall thickness - has not yet been developed.

Hypervelocity impact tests onto CFRP/Al-HC at velocities in the range 4–6 km s⁻¹ were carried out using the two stage Light Gas Gun (LGG) at the University of Kent at Canterbury [11]. The spherical projectile densities (nylon, aluminium, titanium and steels) represented a large range of densities present in LEO and were fired over a wide range of impact angles (0–75°). The combined data are used here to explore scaling of honeycomb damage with an aluminium Whipple bumper equation and the influence of impact angle on the ballistic limit.

The ballistic limit of the target has been identified to be strongly dependent on impact angle; the ballistic limit rose from 25–30 J at normal incidence to 55 J at 15°, then to 156 J for 45° incidence, as identified by marginal perforation of the rear facesheet. This impact angle dependence is greater than that shown by previous tests on honeycomb [4]. An empirically-determined damage law relating the internal areal damage of honeycomb as a function of impact energy for spherical projectiles at incidences of 0°–50° has been derived. The angular spread and composition of debris clouds resulting from perforation of the 47.2 mm target by solid nylon cylindrical projectiles have been characterised. An aluminium Whipple bumper damage equation has been used to predict the ballistic limit for an aluminium target equivalent to the CFRP facesheet and spacing used. Modification of the rear wall thickness to a reduced value is required to bring the 0° and 15° incidence data into agreement with the ballistic limit curve.

MATERIALS AND METHODS

The target material was a honeycomb structure, consisting of CFRP facesheets and an aluminium core (Al-HC), as typically used for a LEO space platform. The CFRP/Al-HC lay-up and material properties are given in Table 1. The shot programme is given in Table 2.

Table 1. Target material

<i>Face sheets</i>	<i>Face sheets</i>	<i>Honeycomb core</i>	<i>Honeycomb core</i>
Prepreg matrix	4 ply satin woven carbon fibre epoxy HMF371-7714B	Section type	Aeroweb
Fibre Orientation	0°/90°/90°/0°	Material	Al Alloy 3003
Thickness	1.62 mm	Core density	83 kg m ⁻³ (5.2 lb ft ⁻³)
Density	1800 - 1850 kg m ⁻³	Cell size	6.4 mm (0.25 inches)
Modulus of Elasticity	69.1 - 69.5 kN mm ⁻²	Cell foil thickness	0.06 mm (25 x 10 ⁻⁴ inches)
		Core thickness	45 mm
		Film adhesive	Redux 609 or 312

Table 2. Shot programme

<i>Parameter</i>	<i>This work + Ref. 12</i>	<i>Ref. 13</i>
d _p (mm)	0.8, 1.0, 1.2, 1.5, 2.0, 4.35	0.8, 1.0, 1.2, 1.5, 2.0
v (km s ⁻¹)	4.71-5.8	4.5-6.2
ρ _n (g cm ⁻³)	1.15, 2.78, 3.99, 4.51, 7.75	1.15, 2.78, 3.99, 4.50, 7.75, 8.47
Θ (°)	0, 15, 30, 45, 60, 75	0
No. shots	28	14

Two mounting arrangements were used for the targets. For the perforating shots, the target was mounted as shown in Fig. 1; held between two aluminium plates, with a witness plate offset at 100 mm behind the target and parallel to the target inclination. The witness plates were manufactured from 2024 Al alloy and were 1 mm thick. The witness plates were between 203 and 286 mm wide and 203 and 273 mm in height and were sized so as to catch the full extent of the debris cloud projected from the rear of the honeycomb target. Higher incidence shots (Θ > 45°) could not be carried out as the witness plates were limited in size by the internal dimensions of the target chamber. For the non-perforating shots, the targets were angled on a support beam and clamped into place. This allowed the positioning of witness plates to catch ricochet ejecta from highly oblique shots.

The target damage morphology is described in Fig. 2. The front and rear holes were digitally imaged and the projected area of the holes (A_{h(front)} and A_{h(rear)}) were calculated via a pixel recognition/counting program and the appropriate scaling factor. By defining the hole damage A_h as an ellipse, the equivalent diameter (D_{eq}) was calculated using Eqn. 1, excluding any delamination damage of the surface. (Delamination damage is defined as material removed around the central hole which does not fully penetrate the surface.) An estimate of the reproducibility of the shots was provided by analysis of two pairs of shots using identical projectiles, impact angles and velocities. The variation in the crater features was used to estimate the 'reproducibility' errors applied to the data.

$$D_{eq} = (4A_h / \pi)^{0.5} \quad (1)$$

The internal honeycomb damage was measured using 30 keV X-rays. A Polaroid film recorded the cell damage integrated over the target thickness. The resulting morphology was compared to that defined in Fig. 3 and the maximum damage area (D_{dam}) was determined using the same technique as for the CFRP hole. Due to the difficulty in accurately estimating the boundaries of the honeycomb damage, an error was placed on each value of D_{dam} to represent operator bias.

The witness plates from the three perforating shots (using solid cylindrical nylon projectiles) were examined under low magnification and the type of damage identified (based on classifications derived in [13]). The diameters of the damaged regions (primary and secondary damage) identified after this classification were measured, as was the deflection of the centre of the damaged region from the line of flight (LOF) of the projectile. These angles and measurements - D_{prim}, D_{sec}, α, β, ε - are defined in Fig. 4. The diameter of the base of the cones was found by averaging the measured diameters in four orthogonal directions; the damaged areas were circular to within 5-10%. The witness plate perforations were also identified and measured.

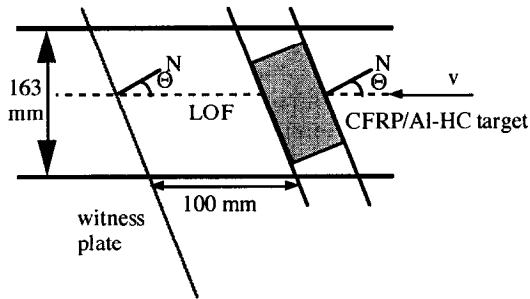


Fig. 1. Target and witness plate mounting

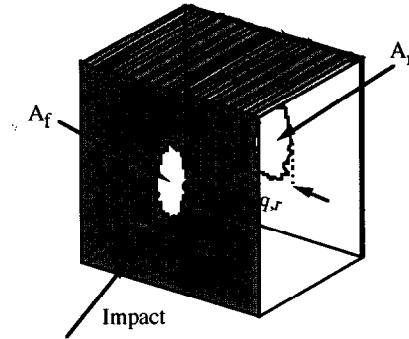


Fig. 2. Target damage parameters

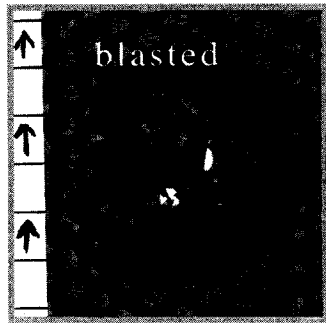


Fig. 3. Internal honeycomb damage morphology. (Definitions from [12])

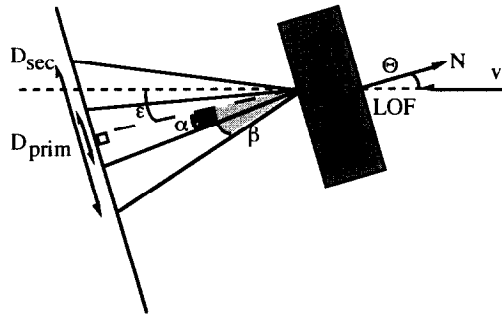


Fig. 4. Debris cloud cone angles

The targets were classified as perforating (rear hole present; beyond the ballistic limit) or non-perforating (no rear hole; below the ballistic limit). The influence of impact angle, impact energy and projectile density for constant impact angle on the ballistic limit was assessed. Previously published impact data on honeycomb were used to determine a ballistic limit scaling factor between normal and oblique incidence impacts, which was compared to the data [4]. The parameter D_{dam} was analysed as a function of the impactor parameters (impact angle, projectile density and impact energy) and a least squares fit carried out between E and D_{dam} . The modified Cour-Palais aluminium Whipple bumper equation [14] was used to predict the critical projectile diameter (d_{crit}) required to perforate the honeycomb-equivalent aluminium Whipple shield (Eqns. 2-4). Eqn. 2 is valid for velocities $< 3 \text{ km s}^{-1}$ and Eqn. 3 is valid for normal impact velocities greater than 7 km s^{-1} . Eqn. 4 represents a linear interpolation between 3 and 7 km s^{-1} . For oblique incidence impacts the normal component of velocity is used to define the regions. The equivalent thickness of aluminium for the CFRP facesheets was calculated by scaling the areal density of CFRP against that of aluminium. The honeycomb core depth was equated to the Whipple bumper spacing, S . A comparison was made between the d_{crit} values estimated and the particle diameters tested to determine how accurate a Whipple bumper equation is at estimating the ballistic limit of a honeycomb target. A modification to the rear wall thickness was applied to bring the normal and near-normal incidence data into agreement with the ballistic limit curve.

$$d_{crit} = \left\{ \left[\frac{t_w \left(\frac{\sigma}{40} \right)^{0.5} + t_b}{(0.6 \rho_p^{0.5} (\cos \Theta)^{5/3} V^{2/3})} \right]^{1.8} \right\}^{1/19} \tag{2}$$

$$d_{crit} = \left\{ \left[3.918 t_w^{2/3} \rho_p^{-1/3} \rho_b^{-1/9} S^{1/3} \left(\frac{\sigma}{70} \right)^{1/3} (V \cos \Theta)^{-2/3} \right] \right\} \tag{3}$$

$$d_{crit} = \left\{ \left[\frac{(t_w \left(\frac{\sigma}{40}\right)^{0.5} + t_b)}{(1.248 \rho_p^{0.5} \cos \Theta)} \right]^{\frac{18}{9}} \left(1.75 \frac{(V \cos \Theta)}{4} \right) \right\} + \left\{ \left[1.071 t_w^{2/3} \rho_p^{-1/3} \rho_b^{-1/9} S^{1/3} \left(\frac{\sigma}{70}\right) \right] \left(\frac{(V \cos \Theta)}{4} - 0.75 \right) \right\} \quad (4)$$

RESULTS AND DISCUSSION

The morphology of the impacts noted on the shots is similar to that noted in previous tests [12, 13]. The circularity of the entrance crater for impacts up to 45 degrees is confirmed (Fig. 5a, c, e). The rear damage for the impacts at ~ 900 J (solid nylon cylindrical projectiles) also includes asymmetric exit holes (Fig. 5d) and facesheet splitting (Fig. 5f). For these impact energies the rear facesheet is on the threshold of delamination from the honeycomb core. The internal honeycomb damage morphology in Fig. 3 (from [12]) is again seen in the solid nylon sabot shots (Fig. 6). The influence of impact angle is seen in the series of shots (0°, 30°, 45°); the arrow signifies the direction of impact. The unusual shape of the honeycomb blast area for the 30° shot could be explained by a slightly rotating impactor (cylinder), although the entrance hole (Fig. 5c) does not show any strong evidence of this. The lighter area at the top of the image denotes the facesheet ‘overhang’ over the honeycomb core; although the honeycomb damage appears truncated, it did not extend beyond the facesheet and no honeycomb damage was visible from the target exterior. Note also that the type of honeycomb damage increases with impact angle: moving from primarily ‘burst’ cells to ‘blasted’ cells. The areal damage also increases by a factor of two from 0° to 30°. There is much more delamination of the core to the facesheet around the entrance and exit holes (superimposed in the X-ray) than noted for earlier shots (Fig. 6 compared to Fig. 3). A summary of the target damage is presented in Table 3.

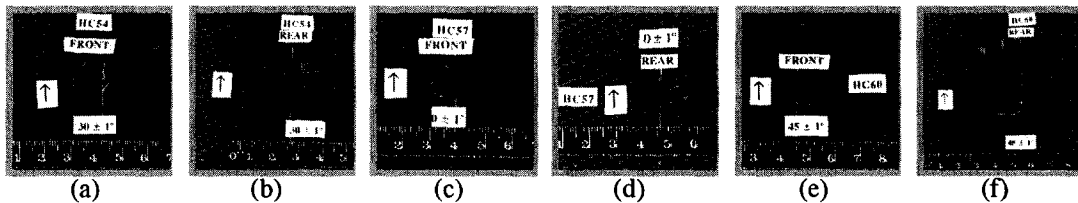


Fig. 5. Target morphologies beyond the ballistic limit as a function of impact angle (solid nylon cylindrical projectile).

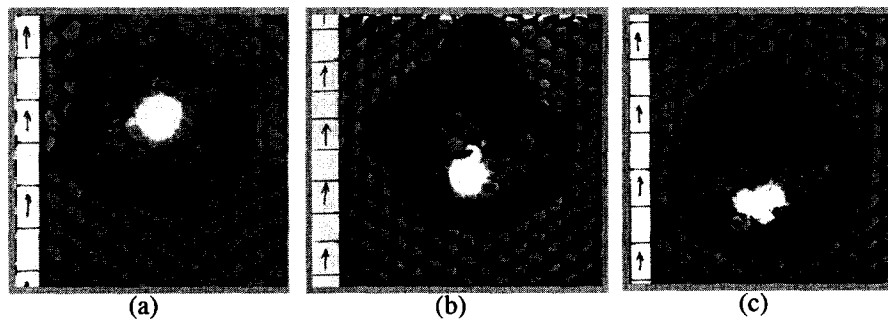


Fig. 6. Honeycomb blast damage. (a) $\Theta = 0^\circ$ (b) $\Theta = 30^\circ$ (c) $\Theta = 45^\circ$.

The impact results for the normal incidence shots are presented in Fig. 7, sorted by impact energy and projectile density. They are divided into perforating (P) and non-perforating (NP) shots. The ballistic limit of the target for aluminium projectiles is between 25 and 30 J, but at an impact energy of 60 J a nylon projectile is below the threshold for perforation of the target. The ballistic limit for a nylon projectile is poorly defined, lying between 60 and ~900 J, as projectile diameters between 2.0 and 4.3 mm (cylinder) cannot be fired in the LGG. The impact tests into a similar target agree well with the results presented [10]. As previously noted, the projectile density at constant impact energy may influence the ballistic limit [13].

Table 3. Results of LGG shots on CFRP/Al-HC honeycomb .
(HC01-HC18 previously published in [13]).

Shot ID	d_p (mm)	ρ_p (g cm ⁻³)	v (km s ⁻¹)	E (J)	θ (°)	D_{eq} (front)	D_{eq} (rear)	Comments
HC01	2.00	7.75	5.87	559	0.0	8.06	9.79	Rear larger than front
HC02	1.00	7.75	6.14	76.5	0.0	2.17	4.05	Rear larger than front
HC03	1.00	8.47	6.23	86.1	0.0	2.71	6.01	Rear larger than front
HC04	1.50	1.45	4.89	30.6	0.0	3.99	none	No rear perforation
HC05	1.50	8.47	5.00	187	0.0	3.56	4.86, 4.40	Rear larger than front, two exit holes
HC06	1.50	7.75	4.95	168	0.0	7.74	7.77	Rear equal to front
HC07	2.00	8.47	4.75	400	0.0	8.31	6.15	Rear smaller than front
HC08	1.00	4.50	4.46	23.4	0.0	3.40	none	No rear perforation
HC11	1.20	1.15	4.62	11.1	0.0	2.76	none	No rear perforation
HC13	2.00	1.15	5.00	60.2	0.0	4.33	none	No rear perforation
HC15	1.00	2.78	5.42	21.4	0.0	2.71	none	No rear perforation
HC16	1.20	2.78	4.86	29.7	0.0	3.51	1.80	Rear smaller than front
HC17	1.50	2.78	5.93	86.4	0.0	3.92	4.77	Rear larger than front
HC18	2.00	2.78	5.08	150	0.0	4.56	6.45	Rear larger than front
HC20	1.50	2.78	4.84	58.0	46.6	5.4	none	No rear perforation
HC21	1.20	2.78	5.23	34.6	44.3	4.2	none	No rear perforation
HC22	1.50	2.78	4.99	61.6	74.6	4.2	none	No rear perforation
HC23	1.20	2.78	4.96	31.2	74.4	3.1	none	No rear perforation
HC24	1.50	3.99	4.73	78.8	74.7	4.3	none	No rear perforation
HC25	1.50	2.78	5.11	64.6	74.7	4.4	none	No rear perforation
HC26	1.20	2.78	4.99	31.5	14.3	3.7	none	No rear perforation
HC27	1.50	2.78	4.94	60.4	14.7	5.0	5.6	Rear larger than front
HC28	0.80	7.75	5.09	26.9	14.4	3.6	none	No rear perforation
HC29	1.00	7.75	5.76	67.3	16.0	3.2	1.6	Rear smaller than front
HC33	1.20	2.78	5.15	33.6	24.5	2.7	none	No rear perforation
HC34	1.20	2.78	5.17	33.9	63.5	3.4	none	No rear perforation
HC35	1.20	2.78	5.24	34.8	59.7	3.9	none	No rear perforation
HC36	1.00	7.75	5.07	52.2	74.4	3.9	none	No rear perforation
HC37	1.00	7.75	5.30	57.0	45.0	4.4	none	No rear perforation
HC38	1.50	3.99	4.91	84.9	45.0	4.6	none	No rear perforation
HC41	1.20	4.51	5.04	51.8	73.4	3.4	none	No rear perforation
HC43	1.20	4.51	5.18	54.7	44.5	4.0	none	No rear perforation
HC44	1.20	4.51	5.06	52.2	17.0	3.7	none	No rear perforation
HC45	1.20	4.51	5.10	53.0	14.8	3.3	none	No rear perforation
HC46	1.20	4.51	5.13	53.7	74.1	3.9	none	No rear perforation
HC47	2.00	2.78	4.71	57.6	130.1	5.2	none	No rear perforation
HC51	2.00	2.78	4.80	16.2	135.1	7.3	3.5	Rear smaller than front
HC54	4.34	1.15	4.80	30.0	886.0	10.3	9.1	Rear smaller than front (cylindrical projectile)
HC57	(L/D = 1.04) 4.34	1.15	4.75	0.0	864.0	13.4	23.7	Rear larger than front (cylindrical projectile)
HC60	(L/D = 1.04) 4.34	1.15	4.82	45.0	890.0	10.2	8.4, 4.9	Rear smaller than front, two exit holes. (cylindrical projectile)
HC61	(L/D = 1.04) 2.00	2.78	5.18	29.2	156.2	5.0	5.4	Rear larger than front
HC62	2.00	2.78	5.19	44.0	156.8	5.4	1.0	Marginal perforation of rear

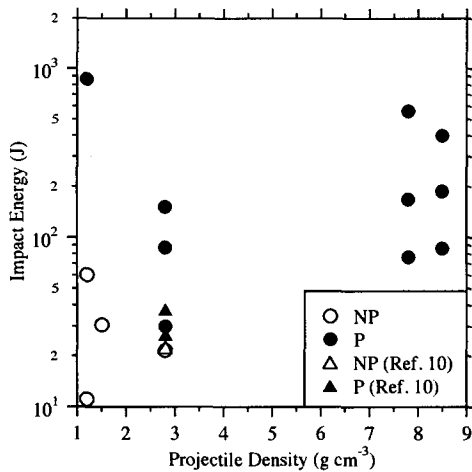


Fig. 7. The dependence of the ballistic limit on impact energy and projectile density for normal incidence impact (NP: non-perforating impact; P: perforating impact)

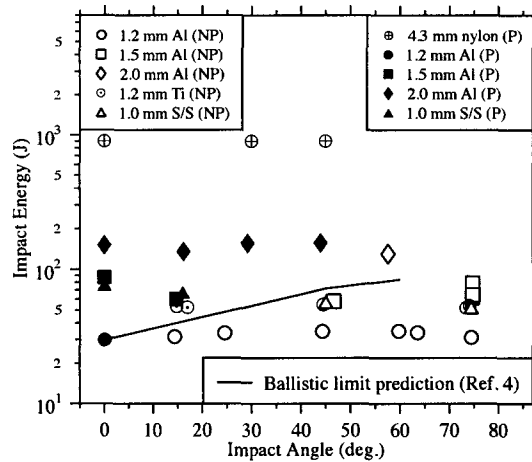


Fig. 8. The dependence of the ballistic limit on impact angle and impact energy. The ballistic limit prediction is scaled from Al/Al-HC data. (NP: non-perforating impact; P: perforating impact).

However, the majority of impacts in space will be at non-normal incidence. The results of some 28 shots, covering a projectile density range of 1.15 to 7.75 g cm⁻³, are plotted in Fig. 8. The ballistic limit of the honeycomb has been observed previously to be affected by the obliquity of the impactor; the line of flight of the projectile will encounter progressively more layers of honeycomb (analogous to ‘thin aluminium bumpers’) as the impact angle is increased [4]. The ballistic limit of the CFRP/Al-HC target increased from 25–30 J to ~55 J as the impact angle was increased from 0 to 15°. The ballistic limit at 45° is well defined at 156 J (the 2 mm projectile just perforating the rear facesheet. At 57° it is greater than ~140 J. As the velocity range of these data is 4.5 and 5.5 km s⁻¹, the influence of velocity on the ballistic limit cannot be evaluated. However, previously-published tests onto an aluminium honeycomb ($t_b = 0.076$ cm, $t_w = 0.051$ cm (both 7075-T6); $S = 2.286$ cm; HC core cell size = 4.76 mm (5052-H39)) which cover a velocity range of 4–8 km s⁻¹ can be used to assess the dependence of the ballistic limit on velocity for one projectile type (a solid Lexan sabot, 4.76 mm diameter, L/D = 1) [4]. Using these data, the impact energies required to reach the ballistic limit of the target at 45° and 60° were calculated to be 2.3 times and 2.8 times that at 0° respectively. These scaling factors are normalised to the impact energy of 30 J (taken from Fig. 7). In Fig. 8, the impact angle dependence predicted by the data in Ref. [4] is not in agreement with the data from this shot programme. The well-defined ballistic limit values at 15° and 45° are under-predicted, with the observed energy at 45° being over twice as large as that predicted by Ref. 4 (69J compared with 156 J). The ballistic limit is again under-predicted by at least 40 J at ~60°. These observed differences may be due to the different shock pressures generated in the projectile and the resulting solid/liquid proportions of the debris cloud (a function of bumper type, thickness and impact velocity), or to the target properties (aluminium versus composite), or, indeed, to the influence of different honeycomb cell core depths.

For four spherical projectile types (1.2, 1.5 mm Al; 1.2 mm Ti; 1.0 mm steel) a series of shots was carried out over the full range of impact angles to explore the effect of impact angle on the honeycomb blast damage area. The impact energies for each projectile type were tightly grouped as the impact velocities were similar. The results are plotted in Fig. 9 and show that, for the range of projectiles tested, the honeycomb damage does not vary significantly for impact angles between 0° and 50°. Above this point, the data tail off rapidly. Therefore, it can be assumed that, for impacts within this range, the damage area at <50° is the same as at 0°. The impact data for these angles are grouped by projectile density in Fig. 10 and show that the four projectile densities are in broad agreement. A damage equation produced by least squares fit to the data (for impact energies between 20 and 400J) for impacts by spherical projectiles is given in Eqn. 5 (E is in joules, D_{dam} in mm²).

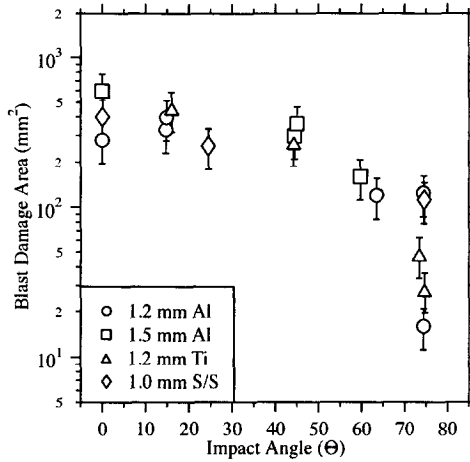


Fig. 9. Honeycomb blast damage area as a function of impact angle for four projectile types at ~ 5 km s⁻¹.

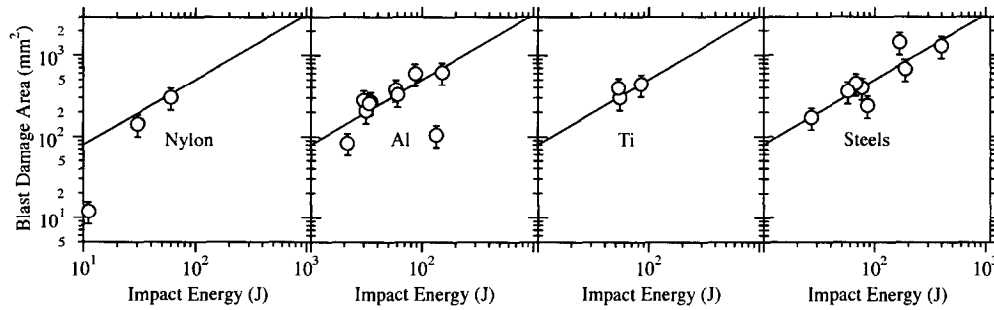


Fig. 10. Honeycomb blast damage for impact angles 0–45°, sorted by projectile density. The line (Eqn. 5) represents a least squares fit to all data with an impact energy < 400 J.

$$D_{\text{dam}} = 10^{1.1 \pm 0.2} E^{0.8 \pm 1.1} \quad (r^2 = 0.8) \quad (5)$$

Table 4. Witness plate angles

Plate	Impact angle Θ ($\pm 5^\circ$)	Primary cone angle α ($\pm 5^\circ$)	Secondary cone angle β ($\pm 5^\circ$)	Turning angle ϵ ($\pm 5^\circ$)
HC57	0	23	43	-6
HC54	30	21	44	36
HC60	45	28	42	48

The primary and secondary ejecta damage morphologies were used to calculate the angles α , β and ϵ . The values of α , β and ϵ are given in Table 4 for the three witness plates studied. Two perforations were also recorded in HC57 (measuring 3x2 mm and 6x2 mm). The features in the primary damage cone α are typically near-circular and represent projectile and honeycomb target fragments travelling at velocities close to that of the original impactor. The secondary damage features are shallower and include carbon fibre fragments from the rear of the cone. The values of α are equal within experimental error for 0° and 30° incidence, then increase at 45°, as expected by comparison with [15]. A sharp dependence on turning angle with impact angle is also recorded (Table 4). The anomalous rotation away from this normal measured for HC 57 is probably due to internal honeycomb effects on the passage of the debris cloud.

Considering the qualitative results above, the functional form for a honeycomb-specific damage equation will include target parameters such as the spacing, front and rear facesheet thicknesses and honeycomb cell size and cell wall thickness, in addition to target material parameters. A

detailed test and modelling programme, varying each of these parameters individually, is required to fix the form and exponent values of such an equation.

A simpler, intermediate approach is to scale the impact data with the modified Cour-Palais Whipple bumper equation, as shown by Eqns. 2-4 [14]. This equation consists of a low velocity part (Eqn. 2) and a high velocity part (Eqn. 3), with a linear interpolation between 3 and 7 km s⁻¹ (Eqn. 4). The performance of the Whipple shield is governed by the state of the debris cloud, consisting of projectile and bumper fragments. In Eqns. 2-4, the normal component of the impact velocity governs the damage potential of the debris cloud. Therefore if the smallest diameter projectile required to reach the ballistic limit for a normal incidence impact is at 3 km s⁻¹, the corresponding velocity for the minimum particle diameter will be at 6 km s⁻¹ for a 60° impact. The minimum particle diameter for the oblique incidence impact will be larger than that for the normal incidence impact. Both the dependence on impact angle and on the spacing (equivalent to honeycomb core depth) may be different for honeycomb, as compared to Whipple bumpers. The dispersion of the debris cloud is hampered by the honeycomb for both normal and oblique incidence impacts, with the normal component of the cloud being channelled by the honeycomb cells. The analysis, of both the debris clouds and the internal honeycomb blast, in the section above shows that the honeycomb affects the development of the debris cloud. This is shown by the increase in particle diameter required to reach the ballistic limit at 5 km s⁻¹, from a 1.2 mm spherical aluminium projectile at normal incidence to a 2 mm projectile of the same density at 45° incidence. The greater damage-causing potential of the debris cloud for the 45° incidence impact (due to the presence of more solid fragments) may be counterbalanced by the presence of the honeycomb. Note that the shock pressures generated in the composite material and projectile cannot be assumed to be the same as for an aluminium-aluminium impact. This also adds uncertainty to the calculation.

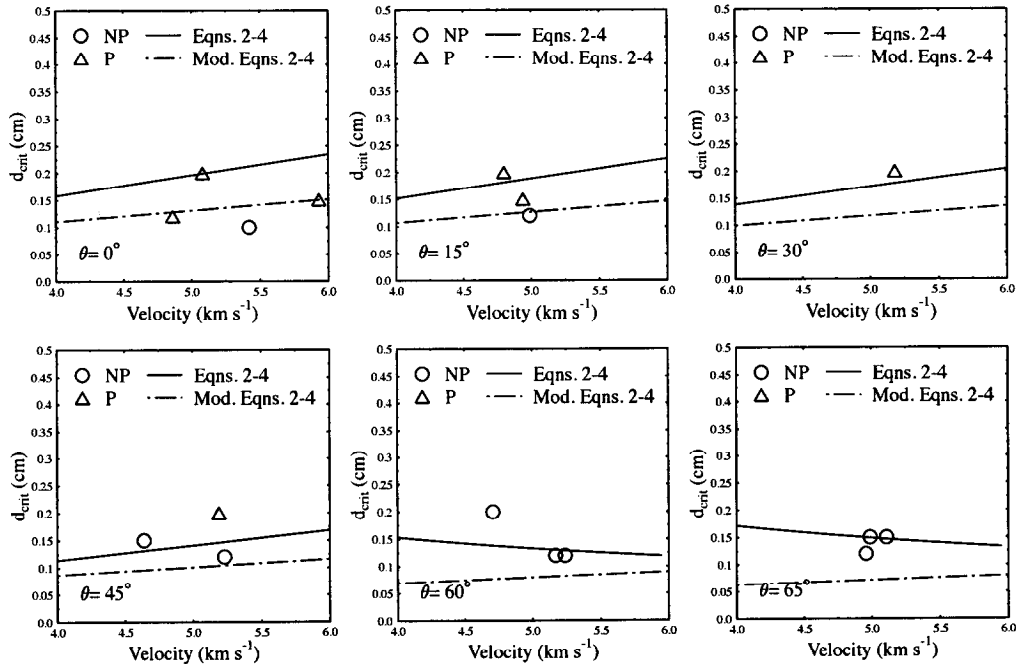


Fig. 11. Modified Cour-Palais Whipple bumper equation predictions compared with aluminium normal and oblique incidence shots. Dashed curve corresponds to ballistic limit curve derived using the scaled rear facesheet thickness.

With these constraints in mind, the impact data (below and above the ballistic limit of the target) can be compared to the Whipple equation predictions for a critical diameter for perforation (d_{crit}). The composite facesheets were converted to equivalent thickness aluminium sheets (1.2 mm thick) and the yield strength values for the front and rear bumpers set to 40 and 70 ksi respectively. For the aluminium impactors in Table 3 (velocity, density, target set-up), the modified Cour-Palais

Whipple bumper equation was used to predict the critical diameter at which the equivalent shield would perforate as a function of velocity (ballistic limit curve). The results for the aluminium projectile data (0° , 15° , 30° , 45° and 60°) are shown in Fig. 11. For the 0° and 15° incidence impacts, the data are below the ballistic limit curve, suggesting that modification of Eqns. 2–4 may be necessary. The 30° and 45° incidence perforating shots are consistent with the curve. However, the non-perforating higher obliquity impacts ($\Theta > 45^\circ$) are above the ballistic limit curve. The performance of the honeycomb is thus conservatively modelled. For normal incidence impacts, the debris cloud has been shown to be ‘channelled’ [15], therefore increasing the areal damage on the rear facesheet (analogous to the rear wall in a Whipple bumper). Therefore it is expected that the shielding effectiveness of the rear facesheets is reduced, compared with a spaced Whipple bumper. A scaling factor has been applied to the modified Cour-Palais Whipple bumper equation in the version implemented in the ESA ESABASE debris modelling software [16]. The rear wall thickness (t_w) can be modified by the use of a scaling factor for both the low and high velocity terms. To bring the normal and near-normal incidence data into agreement with the ballistic limit curve, the rear wall thickness was modified by a scaling factor of 0.5, reducing the effective thickness of the rear facesheet by 50%. The results are again shown in Fig. 11 (dashed curves). Now, the normal incidence perforating shots lie on the scaled ballistic limit curve. For a conservative ballistic limit curve for this honeycomb structure, the value of t_w should be reduced by 50%. Further optimisation of the scaling factor is not recommended, given the number of assumptions made in converting the honeycomb composite facesheet to an equivalent thickness of aluminium.

CONCLUSIONS

The impact response of a 47.2 mm thick CFRP/Al-HC has been characterised as a function of projectile density, impact angle and impact energy for impact energies between 10–1000 J. The energy required to reach the ballistic limit rises with impact angle; it is doubled for impacts going from 0 to 15° incidence. At 5 km s^{-1} , a 1.2 mm aluminium projectile impacting at normal incidence just perforates the rear of the target, whilst a 2 mm projectile is required to perforate at 45° incidence. The honeycomb blast damage area for impacts at equal energies does not significantly change for $\Theta = 0\text{--}50^\circ$, thus an empirically-determined damage law relating the internal areal damage and impact energy for this range of angles has been derived. The debris cone angles for impacts $0\text{--}45^\circ$ have been characterised; the rotation of the cone with respect to the line of flight increases with impact angle, as expected. The modified Cour-Palais aluminium Whipple bumper damage equation has been used to predict the ballistic limit for an aluminium target equivalent to the CFRP facesheet and Al-HC used. A modification to the rear facesheet thickness (as used in the ESA triple wall equation) is required to bring the normal incidence data into line with the ballistic limit curve.

Acknowledgements—Thanks are due to the Particle Physics and Astronomy Research Council (PPARC) for funding of the Light Gas Gun hypervelocity impact facility. E. A. Taylor would like to acknowledge funding from Matra Marconi Space (UK) and the University of Kent at Canterbury. Thanks are also due to Dr. J. Hodgkinson of the Centre for Composite Materials, Imperial College, U. K. for providing the X-ray facilities.

REFERENCES

1. C. C. Poteet, Computational study of hypervelocity impacts on metallic thermal protection systems, *Proc. 8th AIAA International Space Planes and Hypersonic Systems and Technologies Conference*, AIAA-98-1611, pp. 572–584, April 27–30, Norfolk, VI (1998).
2. C. J. Maiden, A. R. McMillan, R. E. Sennett and J. W. Gehring, Experimental investigations of simulated meteoroid damage to various spacecraft structures, *NASA CR-65222* (1965).
3. R. E. Sennett and B. L. Lathrop, Effects of hypervelocity impact on honeycomb structures, *J. Spacecraft and Rockets*, **5**, 1496–1497 (1968).
4. D. W. Jex, A. M. Miller and C. A. Mackay, The characteristics of penetration for a double-sheet structure with honeycomb, *NASA TM X-53974* (1970).
5. D. T. Frate and H. K. Nagra, Hypervelocity impact testing of nickel hydrogen battery cells, *Proc. AIAA Space Programs and Technologies Conference*, AIAA 96-4292, September 24–26, Huntsville, AL (1996).
6. G. L. Shephard and S. A. Scheer, Secondary debris impact damage and environment study, *Int. J. Impact Engng.*, **14**, 671–682 (1993).
7. F. Terrillon, H. R. Warren and M. J. Yelle, Orbital debris shielding design of the Radarsat spacecraft, *42nd International Astronautical Congress*, IAF-91-283, October 5–11, Montreal, Canada (1991).

8. G. A. Sanchez and J. H. Kerr, Advanced X-ray astrophysics facility (AXAF) meteoroid and orbital debris test report, JSC 27354 (1996).
9. C. L. Frost and P. I. Rodriguez, AXAF hypervelocity impact test results, *Proceedings of the Second European Conference on Space Debris*, ESA SP-393, pp. 423-426 (1997).
10. M. Lambert, Hypervelocity impacts and damage laws, *Adv. Space Res.*, **19**(2), 369-378 (1997).
11. M. J. Burchell, M. J. Cole, J. A. M. McDonnell and J. C. Zarnecki, Hypervelocity impact studies using the 2 MV Van de Graaff accelerator and two-stage light gas gun of the University of Kent at Canterbury, *Meas. Sci. Tech.*, in press (1999).
12. E. A. Taylor, M. K. Herbert and L. Kay, Space debris hypervelocity impact on carbon fibre reinforced plastic (CFRP)/Al honeycomb at normal and oblique angles, *Proceedings of the Second European Conference on Space Debris*, ESA SP-393, pp. 429-434 (1997).
13. E. A. Taylor, M. K. Herbert, D. J. Gardner, L. Kay, R. Thomson and M. J. Burchell, Hypervelocity impact on carbon fibre reinforced plastic (CFRP) / aluminium honeycomb, *Proceedings of the Institution of Mechanical Engineers Part G : Journal of Aerospace Engineering*, **221**(Part G), 355-366 (1998).
14. E. L. Christiansen, Design and performance equations for advanced meteoroid and debris shields, *Int. J. Impact Engng.*, **14**, 145-156 (1993).
15. J. W. Gehring, Chapter IX : Engineering Considerations, *High Velocity Impact Phenomena*, (ed. R. Kinslow), pp. 482-489, Academic Press, New York (1970).
16. G. Drolshagen and J. Borde, ESABASE Debris-Meteoroid/Debris Impact Analysis Technical Description, ESA ESTEC, ESABASE-GD-01/1, Noordwijk, Netherlands (1992).